PAPER

Check for updates

Proton-detected fast-magic-angle spinning NMR of paramagnetic inorganic solids†

Jan Blahut, [ID] [a] Ladislav Benda, [ID] [a] Arthur L. Lejeune, [ID] [ab] Kevin J. Sanders, [a] Benjamin Burcher, [b] Erwann Jeanneau, [ID] [c] David Proriol, [ID] [b] Leonor Catita, [b] Pierre-Alain R. Breuil, [ID] [b] Anne-Agathe Quoineaud, [b] Andrew J. Pell [ID] [ad] and Guido Pintacuda [ID] *[a]

Fast (60 kHz) magic angle spinning solid-state NMR allows very sensitive proton detection in highly paramagnetic organometallic powders. We showcase this technique with the complete assignment of ^{1}H and ^{13}C resonances in a high-spin Fe(II) polymerisation catalyst with less than 2 mg of sample at natural abundance.

Introduction

Solid-state NMR has developed as a generally applicable characterization technique, capable of complementing X-ray crystallography, solution NMR and electron microscopy on a wide range of samples in chemistry, materials science and biology.[1–3] ^{1}H-NMR spectroscopy is the most obvious avenue to fast routine characterization of chemical compounds and biomolecules due to the ubiquitous presence of ^{1}H nuclei, their large gyromagnetic ratio γ_H and high natural abundance. Nonetheless, these same properties lead to a strong dipolar coupling network which prevents identification of the different ^{1}H sites and limits the utility of the technique. In the case of paramagnetic samples, the hyperfine interaction of the high-γ ^{1}H nuclei with the unpaired electrons of the paramagnetic center(s) further exacerbates the problem of acquisition and interpretation of the spectra.[4]

A major step forward in solid-state NMR was the development of very fast magic-angle spinning (MAS) probes. Specifically, fast MAS weakens the ^{1}H dipolar coupling networks and allows the direct detection of proton spectra, opening the door for the characterization of hydrogen environments.[5] MAS rates of 60 kHz and above have allowed accelerated data acquisition for the atomic-level description of structure and dynamics of insoluble, non-crystalline or poorly-crystalline samples, from inorganic matrices[6] to viral capsids[7,8] and membrane proteins in lipid bilayers.[9] The improvements associated with fast MAS are particularly evident in samples of paramagnetic molecules,[10–12] where sensitivity and resolution experience a spectacular enhancement as compared to slower rates, allowing efficient detection of previously unobservable nuclei in close proximity to a metal center.[13–15] Despite this impressive progress, however, the advantages of ^{1}H detection remain largely unexplored on highly paramagnetic substances. In fully-protonated paramagnetic molecules, the massive paramagnetic shift anisotropies add to the large homonuclear dipolar couplings so that a significant number of sidebands are observed for some or all of the resonances even at very large spinning rates. Despite notable proofs of concept highlighting the possibility of the detection of ^{1}H resonances,[16–20] the resulting spectra failed to provide a sufficient level of detail necessary for the identification of individual ^{1}H sites. The characterization of paramagnetic organometallic solids has therefore been mainly based on ^{13}C detection techniques,[21–23] for which sensitivity is optimal in larger MAS rotors (*e.g.* 1.9–2.5 mm) at intermediate spinning frequencies (*e.g.* 30–40 kHz). The low natural abundance of ^{13}C causes a problem in particular in chemistry, where isotopic enrichment is not straightforward.

Here, we show that, by using MAS rates of 60 kHz, in combination with tailored RF irradiation schemes and modern computational approaches, it is possible to record and interpret resolved ^{1}H NMR shifts in a powdered sample of a paramagnetic organometallic complex. Specifically, we characterize a tetracoordinated 14-valence-electron high-spin ($S = 2$) Fe(II) complex (**1**, Scheme 1), a newly-synthetized catalyst for unsaturated compound transformations such as olefin oligomerization and polymerization.

^{a}Université de Lyon, Centre de RMN à Très Hauts Champs de Lyon (UMR 5082 – CNRS, ENS Lyon, UCB Lyon 1), 5 rue de la Doua, 69100 Villeurbanne, France. E-mail: guido. pintacuda@ens-lyon.fr
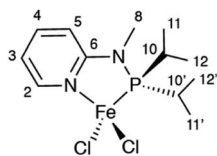
^{b}IFP Energies Nouvelles, Rond-point de l'échangeur de Solaize, 69360 Solaize, France

^{c}Université de Lyon, Centre de Diffractométrie Henri Longchambon (UCB Lyon 1), 5 rue de la Doua, 69100 Villeurbanne, France

^{d}Stockholm University, Department of Materials and Environmental Chemistry, Svante Arrhenius väg 16C, SE-106 91 Stockholm, Sweden

† Electronic supplementary information (ESI) available: Details on sample preparation, NMR spectroscopy; RF pulse sequence schemes; list of chemical shifts; calculation details. CCDC 2063303. For ESI and crystallographic data in CIF or other electronic format see DOI: 10.1039/d1ra04110j

Experimental

Sample preparation

The ligand [*N*-(diisopropylphosphino)-*N*-methylpyridin-2-amine (py-NMe-PiPr$_2$)] in compound **1** was synthetized as

Scheme 1   Structure of complex **1**.

described by Gambarotta's group[24] with yield of 86%. As a Fe(II) source we used $FeCl_2(THF)_{1.5}$ which reacts with 1.05 eq. of py-NMe-PiPr$_2$ in toluene forming **1** in 91% yield as a white powder which was characterized by standard methods including single-crystal X-ray diffraction (see ESI† for details). The obtained XRD unit cell contains eight molecules, two molecules per asymmetric unit.

Solid-state NMR

Solid-state NMR experiments were performed on a Bruker Avance III spectrometer operating at a magnetic field strength of 11.7 T (corresponding to ^{1}H and ^{13}C Larmor frequency of 500.1 and 125.7 MHz) using either a 2.5 mm or a 1.3 mm MAS probe. The sample was packed under inert atmosphere into either a 2.5 mm or a 1.3 mm zirconia rotor and sealed with Vespel rotor caps (estimated sample volume 10 and 2 μL, respectively). In order to improve the seal of the 1.3 mm rotor, FKM inserts were placed between the sample and the caps. Experiments were performed at 31.25 kHz (2.5 mm) or 60 kHz (1.3 mm) MAS (corresponding to a 32 μs and a 16.67 μs rotor period, respectively). The stator was cooled to a temperature of approximately 250 K (31.25 kHz MAS, 3.2 mm) and 260 K (60 kHz MAS, 1.3 mm) using a Bruker BCU XTreme cooling unit, which corresponds to 311.7 ± 0.5 K inside the sample due to frictional heating for the 1.3 mm rotor and similar temperature for the 2.5 mm rotor, as calibrated using δ(^{207}Pb) in crystalline PbNO$_3$,[25] (see ESI†). Temperature variations within the sample were estimated to ±5 K by the same method. Nitrogen gas dried to a dew point of −80 °C was used for sample rotation and temperature regulation.

For experiments in the 2.5 mm and the 1.3 mm probe, the $\pi/2$ ^{1}H pulse lengths used were 1.23 μs at 200 W and 1.1 μs at 30 W, corresponding to RF field strengths of 109 kHz and 227 kHz, respectively. Due to the large span of chemical shifts, short high-powered adiabatic tan h/tan pulses (SHAPs)[26] were used to refocus the chemical shift evolution and invert nuclear spin populations. The adiabatic pulses swept through 5 MHz and were 33.33 μs and 32 μs long, with RF field strengths of 227 kHz and 200 kHz for 31.25 kHz MAS in the 2.5 mm rotor and 60 kHz MAS in the 1.3 mm rotor, respectively. Spectra were acquired with a rotor-synchronized double adiabatic echo experiment with a total double-echo time of 66.68 μs at 60 kHz MAS and 128 μs at 31.25 kHz MAS (four rotor periods). The ^{1}H adiabatic magic angle turning (aMAT)[14] experiment was performed using six adiabatic pulses.

The ^{13}C-detected TEDOR was conducted as in ref. 11 (Fig. 3A), while the new ^{1}H-detected HSQC-TEDOR follows the scheme illustrated in Fig. 3B (for details sequence Fig. S2A and B†).

Due to the requirement of a rotor-synchronized sampling of the indirect dimension (f_1), the spectral width in the indirect ^{13}C dimension is limited by the MAS frequency. In the states-TPPI f_1 acquisition mode, this suppresses the spinning sidebands and removes line-shape distortions,[27] but also produces folding of signals resonating outside this spectral window. The position of the folded resonances was identified by recording a second HSQC-TEDOR spectrum at 58 kHz MAS, i.e., with a 58 kHz ^{13}C spectral widths in f_1. Between the two experiments, any signal folded n-times is shifted by ($n \times \Delta$SW) Hz in the indirect dimension, where ΔSW = 2 kHz is the difference in spectral width between the two experiments. Here, a shift of 2 kHz and 4 kHz for the two C3 and C10 signals appearing respectively at δ(^{1}H) = 44 and 265 ppm allowed to deduce the isotropic δ(^{13}C) shifts of 570 and 1067 ppm, respectively, as illustrated in Fig. S3.†

Quantum chemistry calculations

The XRD structure of complex **1** was subjected to optimization of hydrogen atom positions while keeping all other atoms fixed, employing the hybrid Perdew–Burke–Ernzerhof functional PBE0,[28,29] Grimme's D3 dispersion correction[30] with Becke–Johnson damping,[31] and a locally dense Gaussian basis set using def2-TZVP for Fe and def2-SVP for main group elements[32] as implemented in the TURBOMOLE code.[33] The NMR reference compound tetramethylsilane (TMS) was fully optimized on the same level. All DFT calculations for the Fe(II) complex **1** were done for a quintet ground state.

Electron paramagnetic resonance (EPR) g- and D-tensors were obtained for the hydrogen-optimized XRD structure of complex **1**, applying a strongly contracted variant of the N-electron valence-state perturbation theory of the second order (NEVPT2)[34] to a state-averaged complete-active-space self-consistent-field reference wave-function[35,36] with six electrons in five active 3d-orbitals of Fe(II) (SA-CASSCF(6,5)) as implemented in ORCA.[37] The locally dense basis used in the DFT structure optimizations was enhanced with diffuse functions optimized for molecular property calculations[38] thus employing def2-TZVPD and def2-SVPD bases for Fe and main group elements, respectively. Fermi-contact and spin-dipolar terms of EPR hyperfine coupling tensors for the ^{1}H and ^{13}C nuclei were calculated using a series of hybrid PBE functionals with the admixture of Hartree–Fock exchange ranging from 10 to 40%. GIAO orbital shielding tensors[39] were calculated on the PBE0 level with GAUSSIAN.[40] The hyperfine coupling and orbital shielding calculations employed the def2-TZVPD and IGLO-III[41] atomic bases for Fe and main group elements, respectively. Spin–orbit terms of hyperfine coupling were calculated for all ^{1}H and ^{13}C nuclei using non-hybrid PBE functional and IGLO-II + def2-TZVPD (Fe) basis set. The associated paramagnetic NMR shift corrections were found negligible (Fig. S5,† panel D).

Paramagnetic NMR shift calculations

Hyperfine shielding tensors $\boldsymbol{\sigma}_K^{hf}$ were calculated according to the theory of Kurland & McGarvey[42] in its recent formulation by Vaara et al.[43] where the hyperfine shielding tensor is expressed in terms of EPR property tensors,

$$\boldsymbol{\sigma}_K^{\mathrm{hf}} = -\frac{\mu_{\mathrm{B}}}{kT\hbar\gamma_K}\mathbf{g}\cdot\langle\mathbf{SS}\rangle\cdot\mathbf{A}_K, \tag{1}$$

$$\langle S_u S_v\rangle = \frac{\sum_{mn}Q_{mn}\langle n|S_u|m\rangle\langle m|S_v|n\rangle}{\sum_n\exp(-E_n/kT)}, \quad u,v=\{x,y,z\}$$

$$Q_{mn} = \begin{cases} \mathrm{e}^{-E_n/kT} & , \ E_n = E_m \\ -\dfrac{kT}{E_m - E_n}\left[\mathrm{e}^{-E_m/kT} - \mathrm{e}^{-E_n/kT}\right] & , \ E_n \neq E_m \end{cases}.$$

Isotropic paramagnetic NMR shielding was obtained as the isotropic value of the total (orbital plus hyperfine) shielding tensor,

$$\sigma_K = \frac{1}{3}\mathrm{Tr}\left(\boldsymbol{\sigma}_K^{\mathrm{orb}} + \boldsymbol{\sigma}_K^{\mathrm{hf}}\right).$$

Finally, paramagnetic NMR shifts were calculated as $\delta_K = \sigma_K^{\mathrm{ref}} - \sigma_K$ where the values of calculated reference shielding σ_K^{ref} in TMS were 31.6 and 185.7 ppm for ^{1}H and ^{13}C nuclei, respectively.[44] Intermolecular pseudo-contact shifts (PCS) in molecular crystal of complex **1** were included by periodically extending the XRD unit cell and collecting contributions from all paramagnetic Fe(II) centers within 40 Å from the central Fe(II) ion (645 contributions to each NMR shift).

Individual PCS contributions $\delta_{K,i}^{\mathrm{pc}}$ were calculated with a classical dipolar approximation

$$\delta_{K,i}^{\mathrm{pc}} = \frac{1}{12\pi\mathrm{r}_{KS_i}^{3}}\mathrm{Tr}\left[\Delta\boldsymbol{\chi}_i\cdot\left(\frac{3\mathbf{r}_{KS_i}\mathbf{r}_{KS_i}}{\mathrm{r}_{KS_i}^{2}} - \mathbf{1}\right)\right] \tag{2}$$

where $\mathbf{r}_{KS_i}$ is the vector connecting nucleus K and a paramagnetic center S_i, **1** is a Cartesian unit matrix, and the paramagnetic susceptibility anisotropy tensors $\Delta\boldsymbol{\chi}_i$ are appropriate rotations of the central tensor $\Delta\boldsymbol{\chi}$ calculated according to the formula[4]

$$\Delta\boldsymbol{\chi} = \frac{\mu_0\mu_{\mathrm{B}}^{2}}{kT}\mathbf{g}\cdot\langle\mathbf{SS}\rangle\cdot\mathbf{g}^{T} \tag{3}$$

that was recently re-derived by applying the dipolar approximation also to spin–orbit and gauge corrections terms of hyperfine coupling tensor $\mathbf{A}_K$ in eqn (1).[45] We note that the spin–orbit corrections to intramolecular hyperfine shifts of complex **1** were calculated explicitly in this work and were found negligible. This suggests that applying the dipolar approximation to HFC terms beyond the leading order, albeit theoretically sound, might in practice represent an inferior treatment to just neglecting the higher order hyperfine coupling terms.

Results and discussion

Fig. 1a shows a ^{1}H spin–echo spectrum acquired under standard conditions for ^{13}C detection, namely moderately fast MAS rate of 31.25 kHz, achievable with a 2.5 mm rotor. Due to the large anisotropy of the paramagnetic ^{1}H shifts and of the ^{1}H–^{1}H
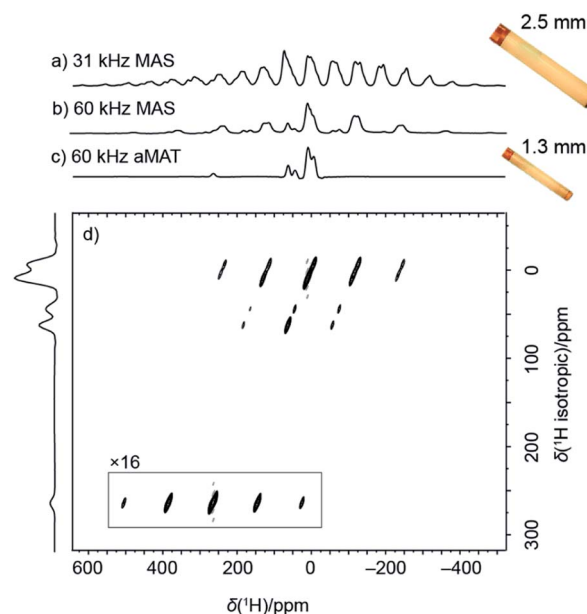

Fig. 1 Solid-state ^{1}H MAS NMR spectra of **1** acquired (a) at 31.25 kHz MAS using a 2.5 mm rotor (internal volume of 10 µL) with a sample temperature of *ca.* 315 K, (b) at 60 kHz MAS using a 1.3 mm rotor (internal volume of 2 µL) with sample temperature of *ca.* 312 K, and (c) a projection of the aMAT spectrum onto the indirect dimension containing only the isotropic resonances. (d) Two-dimensional ^{1}H aMAT experiment of **1** acquired at 60 kHz MAS using a 1.3 mm rotor with a sample temperature of *ca.* 312 K. The direct and indirect dimensions contain the spinning-sideband manifold and the isotropic resonances only, respectively. All experiments were recorded at 11.7 T.

dipolar couplings, the spectrum consists of broad isotropic resonances overlapping with spinning sidebands. The overlap of isotropic signals with spinning side bands is partially removed by spinning the sample at 60 kHz MAS in a smaller 1.3 mm rotor (Fig. 1b). Fast MAS suppresses the intensity and number of spinning sidebands, concentrating more intensity in the center band, and at the same time, allows to reduce the duration of the spin–echo required for the undistorted acquisition of the large spectrum.

Altogether, in addition to the resolution improvement, this produces a sensitivity increase. Interestingly here, the signal intensity of the center-band signals is conserved despite a five-fold smaller sample volume (signal-to-noise ratio normalized by square root of number of scans is 16.7 and 14.9 for 2.5 mm and 1.3 mm rotors respectively, for the dominant center band at 10 ppm).

An additional effort is however still needed for the unambiguous identification of the individual isotropic ^{1}H resonances. This is provided by a 2D sideband separation experiment such as the adiabatic Magic Angle Turning (aMAT) sequence,[14] which uses a train of adiabatic refocusing pulses[46] with unique timings in order to result in pure isotropic evolution in the indirect dimension. The experiment, originally developed for lower-γ nuclei in the context of energy storage materials,[47–50] achieves a 2D spectrum correlating pure isotropic to anisotropic frequencies (Fig. 1d), with a projection along the indirect dimension (Fig. 1c) featuring greatly enhanced spectral
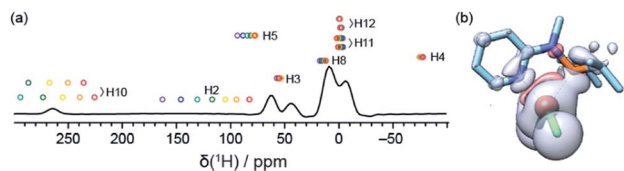
Fig. 2 (a) Projection of the indirect dimension of the ^{1}H aMAT experiment of 1 acquired at 60 kHz MAS and 11.7 T in a 1.3 mm rotor with a sample temperature of *ca.* 312 K. Rainbow-colored circles correspond to calculated shifts using different Hartree–Fock exchange admixtures in hybrid DFT functional used for hyperfine coupling calculations, ranging from 10% (purple) to 40% (red). Signals of the CH groups 2 and 4 were not observed due to rapid ^{1}H relaxation during the aMAT evolution delay. The calculated shifts for H10, ranging from 394 ppm (10%) to 220 ppm (40%), are shown only partially. (b) Outer contour of unpaired electron density (right; dark blue 0.0005 a.u. and red −0.0005 a.u.) calculated by DFT using a 25% Hartree–Fock exchange admixture. Hydrogen atoms are omitted for clarity.

resolution. Only 54 minutes were required for the acquisition of such correlation, and notably, despite linewidths of 5 to 9 kHz, several well-resolved resonances could be identified, distributed over a broad spectral range between 300 and −25 ppm.

These resonances can be interpreted on the basis of the paramagnetic shifts predicted from the crystal structure of **1**. Rigorous quantum chemistry prediction of paramagnetic shifts including the effects of spin–orbit coupling has been enabled by recent theory developments within the Kurland–McGarvey framework.[42,43,51] Paramagnetic shifts are calculated with an uncertainty associated with the problem of density functional theory (DFT) with reliably quantifying contact hyperfine interactions.[52] Adjusting the admixture of Hartree–Fock exchange (HFX) in hybrid DFT calculations offers a means to probe this uncertainty.[53–56] In Fig. 2a, colored circles correspond to the shifts calculated with hybrid PBE functional with HFX percentage ranging from 10 to 40%. By comparing experimental ^{1}H spectrum and predictions, some resonances (H3, H5, H10) can be readily assigned within the confidence intervals provided by the set of multiple-level calculations. Note that the predicted range of shifts is very narrow for some resonances (H8, H11, and H12), which allows a tentative assignment despite the crowding and overlap in that region. This result already demonstrates the possibility of an atomic-level characterization of such challenging samples at natural abundance.

The contrasting scale of response of different atoms to the variation of HFX admixture demonstrates the difficulty of the problem at hand. Propagation of unpaired electron density across several bonds from the metal to the ligand atoms (Fig. 2b) needs to be described very accurately for a reliable calculation of (Fermi-) contact hyperfine coupling. For example, high spin-density regions are visible for hydrogen atoms at position 10, which correspond to the largest ^{1}H shift observed in the experiments. However, in the absence of a benchmark multi-reference *ab initio* method for hyperfine couplings we are limited to non-benchmarked, inherently single-reference DFT. The contrasting response of hyperfine shifts to the HFX admixture variation is thus not much surprising: unpaired
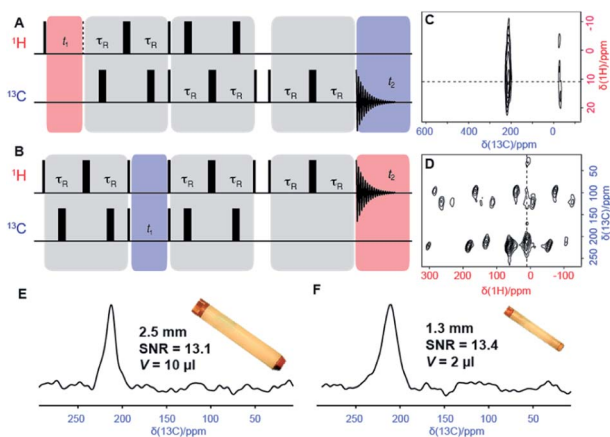

Fig. 3 (A and B) Pulse sequences of the two-dimensional TEDOR experiment for correlating nearby ^{1}H and ^{13}C nuclei. The sequence in (A) is designed for ^{13}C detection and referred to as TEDOR. It consists of a ^{1}H excitation pulse followed by t_1 evolution and a first recoupling block, then after a magnetization transfer, a second recoupling block is applied to refocus observable ^{13}C coherences. A z-filtered echoed detection is used as described by Kervern *et al.*[11] The ^{1}H detected experiment is performed using the sequence shown in (B), and referred to as HSQC-TEDOR. The ^{13}C evolution period is interleaved with two REDOR blocks used to refocus ^{1}H coherences by reintroducing CH dipolar couplings. ^{1}H coherences are detected after a z-filter and an echo. (C and D) Experimental TEDOR spectra with ^{13}C detection (C), acquired at 31.25 kHz using a 2.5 mm rotor, and with ^{1}H detection (D), acquired at 60 kHz using a 1.3 mm rotor. Both spectra were recorded in an external magnetic field of 11.7 T. Narrow and broad black rectangles denote π/2 and π pulses, respectively. Experimental times were about 13 h and 11 h respectively. (E and F) ^{13}C slices from spectra shown in C and D extracted at $\delta_{1H} = 11$ ppm.

electron density distribution obtained with a generic DFT functional not designed to capture such details may be differently sensitive to HFX admixtures in different parts of the molecule. We also note that, due to the described limitation, randomly trying out different DFT functionals would not be a useful approach. On the contrary, using a single, well-chosen DFT exchange and correlation functional removes one unnecessary degree of freedom that might otherwise obscure the view. PBE exchange and correlation functional used here is arguably the most robust choice for transition metal complexes at large.

Given the spectral overlap of the resonances H8, H11 and H12 (Fig. 2), however, a C–H correlation spectrum would clearly be beneficial for a more extensive characterization. A major step towards assignment of resonances in small to medium-sized paramagnetic complexes was the development of heteronuclear correlations.[11] These experiments achieve transfer of polarization from protons to nearby hetero-nuclei *via* dipolar-recoupling sequences such as Transferred-Echo DOuble Resonance sequence (TEDOR)[57] (Fig. 3a) that use short, high-powered RF pulses. Unlike cross-polarization transfer,[58] this technique allows efficient magnetization transfer for nuclei exposed to strong paramagnetic shift and fast paramagnetic-induced relaxation.[11]

Here, the improved resolution at fast MAS enables the implementation of ^{1}H-detected variants of TEDOR. Fig. 3b
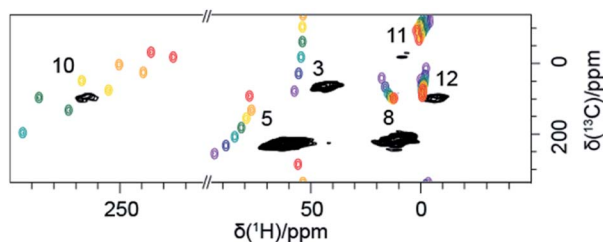
Fig. 4 ^{1}H-detected HSQC-TEDOR spectrum of **1** acquired at 60 kHz and 11.7 T using a 1.3 mm rotor (black) compared with calculated ^{1}H–^{13}C signals using a variable Hartree–Fock exchange admixture for hyperfine coupling (rainbow plot). The spinning sidebands are found in the region of the spectrum with ^{1}H shifts from 80 to 200 ppm, excised here for clarity. Correlations of the CH groups 2 and 4 were not observed due to rapid ^{1}H relaxation. For C3 and C10 (folded resonances), respectively one and two multiples of the spinning frequencies were added to the calculated ^{13}C frequencies so that the calculated shifts appear with in the experimental spectral window.

shows an example of pulse sequence for recording a 2D Dipolar Heteronuclear Single-Quantum Correlation through TEDOR recoupling (HSQC-TEDOR). This pulse sequence provides identical sensitivity to the ^{13}C-detected spectrum acquired at slower MAS even though a five times larger sample volume was used in the latter case. This improvement is ascribed to the shorter recoupling times made possible with faster MAS, which is notably not efficient in the 30 kHz range.[19]

Finally, Fig. 4 shows the 2D H–C correlation spectrum of **1**, exhibiting six correlations out of a total of eight H–C pairs (note that the non-symmetrical environment in the molecular crystal of **1** exposes each nucleus to different paramagnetic effects from several metal centres, making the two *i*Pr moieties magnetically inequivalent and leading to peak doubling for C10 and C11, Fig. S4†). The spectral width in the indirect ^{13}C dimension is limited by the MAS frequency in order to suppress the spinning sidebands and to remove line-shape distortions.[27] This causes folding of the two most shifted signals (C3 and C10), whose position can however be easily deduced by recoding a second spectrum with a slightly different (±2 kHz) MAS rate (see ESI†). Overlaid with the experimental data are the computed shifts for each ^{1}H–^{13}C correlation, again calculated with a hybrid PBE functional with HFX percentage ranging from 10 to 40%. The overall agreement between calculated and experimental shifts permits a full assignment of all observed resonances (a summary of the calculated values and experimental shifts, together with the assignment, is given in Table S3†).

We note that the representation of calculated shifts in the form of a 2D "rainbow plot" on top of the experimental signals allows a direct, rapid and visual evaluation of the performance of the modelling approach chosen and guiding the choice of the most appropriate model. For example, here this graphic representation was used to systematically rate the importance of various secondary effects on the calculated shifts (see ESI, Fig. S5†). Molecular geometry is clearly an important underlying factor and an accurate, well-reasoned geometry treatment is indispensable. Here we compared the periodic X-ray structure with optimised hydrogens to a *in vacuo* fully-optimised

structure, finding that the agreement of certain shifts is improved by full optimisation, while for other shifts the X-ray structure gives better agreement. This indicates that an even better prediction would possibly be achievable with a structure fully-optimised in a crystal lattice, on a dispersion-corrected hybrid DFT level. The contribution of inter-molecular PCS is also important, but only for the atoms in close proximity to the neighbouring Fe^{II} centres. Finally, calculations allow to estimate that the effect of a temperature variation comparable to the experimental variation (here ±5 K) is negligible.

Conclusion

In summary, the results above aim to establish the new state of the art in solid-state NMR spectroscopy applied to paramagnetic organometallic complexes. With the use of 60 kHz MAS, an experimental "toolkit" allowed to achieve (i) broadband acquisition of a ^{1}H spectrum of a paramagnetic powdered complex, (ii) isotropic resolution by the removal of spinning sidebands, and (iii) broadband heteronuclear correlations. The combination of carefully-tuned pulse sequences and high MAS rates permits extensive experimental constraints for resonance assignment, and marked improvements in sensitivity and resolution, allowing a reduction in sample quantities and experiment time for obtaining NMR spectra of paramagnetic materials. We anticipate that the continued development of MAS probes capable of ever higher MAS rates and of the associated RF schemes will extend the horizons of experimental NMR and allow the study of even more complicated systems.

Author contributions

Project design (JB, PAB, AAQ, AJP, GP), funding acquisition (PAB, AAQ, GP), design of NMR methodology (JB, ALL, KJS, AJP, LB, GP), sample preparation and characterization (BB, EJ, DP, PAB), NMR data acquisition and analysis (JB, LB, ALL, KJS), supervision and validation (LC, DP, PAB, AAQ, GP), writing – original draft (JB, LB, ALL, AJP, GP), writing – review & editing (all coauthors).

Conflicts of interest

There are no conflicts to declare.

Acknowledgements

Notes and references

1 Y. C. Su, L. B. Andreas and R. G. Griffin, *Annu. Rev. Biochem.*, 2015, **84**, 465–497.
2 S. E. Ashbrook and P. Hodgkinson, *J. Chem. Phys.*, 2018, **149**, 040901–040914.

© 2021 The Author(s). Published by the Royal Society of Chemistry

3   B. F. Chmelka, *J. Magn. Reson.*, 2019, **306**, 91–97.

4   A. J. Pell, G. Pintacuda and C. P. Grey, *Prog. Nucl. Magn. Reson. Spectrosc.*, 2019, **111**, 1–271.

5   Y. Ishii, J. P. Yesinowski and R. Tycko, *J. Am. Chem. Soc.*, 2001, **123**, 2921–2922.

6   T. Kobayashi, K. Mao, P. Paluch, A. Nowak-Krol, J. Sniechowska, Y. Nishiyama, D. T. Gryko, M. J. Potrzebowski and M. Pruski, *Angew. Chem., Int. Ed.*, 2013, **52**, 14108–14111.

7   L. B. Andreas, K. Jaudzems, J. Stanek, D. Lalli, A. Bertarello, T. Le Marchand, D. Cala-De Paepe, S. Kotelovica, I. Akopjana, B. Knott, S. Wegner, F. Engelke, A. Lesage, L. Emsley, K. Tars, T. Herrmann and G. Pintacuda, *Proc. Natl. Acad. Sci. U. S. A.*, 2016, **113**, 9187–9192.

8   J. Struppe, C. M. Quinn, M. Lu, M. Wang, G. Hou, X. Lu, J. Kraus, L. B. Andreas, J. Stanek, D. Lalli, A. Lesage, G. Pintacuda, W. Maas, A. M. Gronenborn and T. Polenova, *Solid State Nucl. Magn. Reson.*, 2017, **87**, 117–125.

9   T. Schubeis, T. Le Marchand, C. Daday, W. Kopec, K. T. Movellan, J. Stanek, T. S. Schwarzer, K. Castiglione, B. L. de Groot and L. B. Andreas, *Proc. Natl. Acad. Sci. U. S. A.*, 2020, **117**, 21014–21021.

10 Y. Ishii, N. P. Wickramasinghe and S. Chimon, *J. Am. Chem. Soc.*, 2003, **125**, 3438–3439.

11 G. Kervern, G. Pintacuda, Y. Zhang, E. Oldfield, C. Roukoss, E. Kuntz, E. Herdtweck, J.-M. Basset, S. Cadars, A. Lesage, C. Copéret and L. Emsley, *J. Am. Chem. Soc.*, 2006, **128**, 13545–13552.

12 G. Kervern, A. D'Aléo, L. Toupet, O. Maury, L. Emsley and G. Pintacuda, *Angew. Chem., Int. Ed.*, 2009, **48**, 3082–3086.

13 I. Bertini, L. Emsley, M. Lelli, C. Luchinat, J. Mao and G. Pintacuda, *J. Am. Chem. Soc.*, 2010, **132**, 5558–5559.

14 R. J. Clement, A. J. Pell, D. S. Middlemiss, F. C. Strobridge, J. K. Miller, M. S. Whittingham, L. Emsley, C. P. Grey and G. Pintacuda, *J. Am. Chem. Soc.*, 2012, **134**, 17178–17185.

15 A. Bertarello, T. Schubeis, C. Fuccio, E. Ravera, M. Fragai, G. Parigi, L. Emsley, G. Pintacuda and C. Luchinat, *Inorg. Chem.*, 2017, **56**, 6624–6629.

16 N. P. Wickramasinghe, M. Shaibat and Y. Ishii, *J. Am. Chem. Soc.*, 2005, **127**, 5796–5797.

17 G. Kervern, S. Steuernagel, F. Engelke, G. Pintacuda and L. Emsley, *J. Am. Chem. Soc.*, 2007, **129**, 14118–14119.

18 N. P. Wickramasinghe, M. A. Shaibat, C. R. Jones, L. B. Casabianca, A. C. de Dios, J. S. Harwood and Y. Ishii, *J. Chem. Phys.*, 2008, **128**, 052210.

19 S. K. Kumara Swamy, A. Karczmarska, M. Makowska-Janusik, A. Kassiba and J. Dittmer, *ChemPhysChem*, 2013, **14**, 1864–1870.

20 K. Levin and S. Kroeker, *Solid State Nucl. Magn. Reson.*, 2019, **101**, 101–109.

21 D. M. Dawson, L. E. Jamieson, M. I. Mohideen, A. C. McKinlay, I. A. Smellie, R. Cadou, N. S. Keddie, R. E. Morris and S. E. Ashbrook, *Phys. Chem. Chem. Phys.*, 2013, **15**, 919–929.

22 B. Burcher, K. J. Sanders, L. Benda, G. Pintacuda, E. Jeanneau, A. A. Danopoulos, P. Braunstein, H. Olivier-Bourbigou and P. R. Breuil, *Organometallics*, 2017, **36**, 605–613.

23 D. M. Dawson, C. E. F. Sansome, L. N. McHugh, M. J. McPherson, L. J. McCormick McPherson, R. E. Morris and S. E. Ashbrook, *Solid State Nucl. Magn. Reson.*, 2019, **101**, 44–50.

24 Y. Yang, J. Gurnham, B. Liu, R. Duchateau, S. Gambarotta and I. Korobkov, *Organometallics*, 2014, **33**, 5749–5757.

25 A. Bielecki and D. P. Burum, *J. Magn. Reson., Ser. A*, 1995, **116**, 215–220.

26 A. J. Pell and G. Pintacuda, *Prog. Nucl. Magn. Reson. Spectrosc.*, 2015, **84–85**, 33–72.

27 R. Tycko, D. P. Weliky and A. E. Berger, *J. Chem. Phys.*, 1996, **105**, 7915.

28 J. P. Perdew, K. Burke and M. Ernzerhof, *Phys. Rev. Lett.*, 1996, **77**, 3865–3868.

29 J. P. Perdew, M. Ernzerhof and K. Burke, *J. Chem. Phys.*, 1996, **105**, 9982–9985.

30 S. Grimme, J. Antony, S. Ehrlich and H. Krieg, *J. Chem. Phys.*, 2010, 132.

31 S. Grimme, S. Ehrlich and L. Goerigk, *J. Comput. Chem.*, 2011, **32**, 1456–1465.

32 F. Weigend and R. Ahlrichs, *Phys. Chem. Chem. Phys.*, 2005, **7**, 3297.

33 R. Ahlrichs, M. K. Armbruster, R. A. Bachorz, M. Bär, H.-P. Baron, R. Bauernschmitt, F. A. Bischoff, S. Böcker, N. Crawford, P. Deglmann, F. Della Sala, M. Diedenhofen, M. Ehrig, K. Eichkorn, S. Elliot, F. Furche, A. Glöß, F. Haase, M. Häser, C. Hättig, A. Hellweg, S. Höfener, H. Horn, C. Huber, U. Huniar, M. Kattannek, W. Klopper, A. Köhn, C. Kölmel, M. Kollwitz, K. May, P. Nava, C. Ochsenfeld, H. Öhm, M. Pabst, H. Patzelt, D. Rappoport, O. Rubner, A. Schäfer, U. Schneider, M. Sierka, D. P. Tew, O. Treutler, B. Unterreiner, M. von Arnim, F. Weigend, P. Weis, H. Weiss and N. Winter, *Turbomole 6.3.1*, 2011.

34 C. Angeli, R. Cimiraglia, S. Evangelisti, T. Leininger and J. P. Malrieu, *J. Chem. Phys.*, 2001, **114**, 10252–10264.

35 B. O. Roos, P. R. Taylor and P. E. M. Sigbahn, *Chem. Phys.*, 1980, **48**, 157–173.

36 P.-Å. Malmqvist and B. O. Roos, *Chem. Phys. Lett.*, 1989, **155**, 189–194.

37 F. Neese, *Wiley Interdiscip. Rev.: Comput. Mol. Sci.*, 2018, **8**, e1327.

38 D. Rappoport and F. Furche, *J. Chem. Phys.*, 2010, **133**, 134105.

39 K. Wolinski, J. F. Hinton and P. Pulay, *J. Am. Chem. Soc.*, 1990, **112**, 8251–8260.

40 M. J. Frisch, G. W. Trucks, H. B. Schlegel, G. E. Scuseria, M. A. Robb, J. R. Cheeseman, G. Scalmani, V. Barone, B. Mennucci, G. A. Petersson, H. Nakatsuji, M. Caricato, X. Li, H. P. Hratchian, A. F. Izmaylov, J. Bloino, G. Zheng, J. L. Sonnenberg, M. Hada, M. Ehara, K. Toyota, R. Fukuda, J. Hasegawa, M. Ishida, T. Nakajima, Y. Honda, O. Kitao, H. Nakai, T. Vreven, J. A. Montgomery Jr, J. E. Peralta, F. Ogliaro, M. J. Bearpark, J. Heyd, E. N. Brothers, K. N. Kudin, V. N. Staroverov, R. Kobayashi,

J. Normand, K. Raghavachari, A. P. Rendell, J. C. Burant, S. S. Iyengar, J. Tomasi, M. Cossi, N. Rega, N. J. Millam, M. Klene, J. E. Knox, J. B. Cross, V. Bakken, C. Adamo, J. Jaramillo, R. Gomperts, R. E. Stratmann, O. Yazyev, A. J. Austin, R. Cammi, C. Pomelli, J. W. Ochterski, R. L. Martin, K. Morokuma, V. G. Zakrzewski, G. A. Voth, P. Salvador, J. J. Dannenberg, S. Dapprich, A. D. Daniels, Ö. Farkas, J. B. Foresman, J. V. Ortiz, J. Cioslowski and D. J. Fox, *Gaussian 09, revision D.01*, 2009.

41 W. Kutzelnigg, U. Fleischer and M. Schindler, in *NMR - Basic Principles and Progress*, Springer, Heidelberg, 1990, vol. 23, pp. 165–262.

42 R. J. Kurland and B. R. McGarvey, *J. Magn. Reson.*, 1970, **2**, 286–301.

43 J. Vaara, S. A. Rouf and J. Mareš, *J. Chem. Theory Comput.*, 2015, **11**, 4840–4849.

44 A. Bertarello, L. Benda, K. J. Sanders, A. J. Pell, M. J. Knight, V. Pelmenschikov, L. Gonnelli, I. C. Felli, M. Kaupp, L. Emsley, R. Pierattelli and G. Pintacuda, *J. Am. Chem. Soc.*, 2020, **142**, 16757–16765.

45 L. Lang, E. Ravera, G. Parigi, C. Luchinat and F. Neese, *J. Phys. Chem. Lett.*, 2020, **11**, 8735–8744.

46 G. Kervern, G. Pintacuda and L. Emsley, *Chem. Phys. Lett.*, 2007, **435**, 157–162.

47 F. C. Strobridge, D. S. Middlemiss, A. J. Pell, M. Leskes, R. J. Clément, F. Pourpoint, Z. Lu, J. V. Hanna, G. Pintacuda, L. Emsley, A. Samosond and C. P. Grey, *J. Mat. Chem. A*, 2014, **2**, 11948–11957.

48 J. Xu, D. H. Lee, R. J. Clément, X. Yu, M. Leskes, A. J. Pell, G. Pintacuda, X.-Q. Yang, C. P. Grey and Y. S. Meng, *Chem. Mater.*, 2014, **26**, 1260–1269.

49 E. Mitoudi-Vagourdi, W. Papawassiliou, S. Müllner, A. Jaworski, A. J. Pell, P. Lemmens, R. K. Kremer and M. Johnsson, *Inorg. Chem.*, 2018, **57**, 4640–4648.

50 W. Papawassiliou, A. Jaworski, A. J. Pell, J. H. Jang, Y. Kim, S.-C. Lee, H. J. Kim, Y. Alwahedi, S. Alhassan, A. Subrati, M. Fardis, M. Karagianni, N. Panopoulos, J. Dolinšek and G. Papavassiliou, *Nature Comm*, 2020, **11**, 1285.

51 W. Van den Heuvel and A. Soncini, *Phys. Rev. Lett.*, 2012, **109**, 073001.

52 M. Munzarová and M. Kaupp, *J. Phys. Chem. A*, 1999, **103**, 9966–9983.

53 C. Remenyi, R. Reviakine and M. Kaupp, *J. Phys. Chem. A*, 2006, **110**, 4021–4033.

54 C. Remenyi, R. Reviakine and M. Kaupp, *J. Phys. Chem. B*, 2007, **111**, 8290–8304.

55 A. Mondal and M. Kaupp, *J. Phys. Chem. Lett.*, 2018, **9**, 1480–1484.

56 A. Mondal and M. Kaupp, *J. Phys. Chem. C*, 2019, **123**, 8387–8405.

57 A. W. Hing, S. Vega and J. Schaefer, *J. Magn. Reson.*, 1992, **96**, 205–209.

58 S. Li, J. Trébosc, O. Lafon, L. Zhou, M. Shen, F. Pourpoint, J.-P. Amoureux and F. Deng, *J. Magn. Reson.*, 2015, **251**, 36–42.